THE ASTROPHYSICAL JOURNAL, 538:456–466, 2000 July 20

ELECTRON-CYCLOTRON MASER DRIVEN BY CHARGED-PARTICLE ACCELERATION FROM MAGNETIC FIELD–ALIGNED ELECTRIC FIELDS

R. E. ERGUN,[1] C. W. CARLSON, J. P. MCFADDEN, AND G. T. DELORY
Space Sciences Laboratory, University of California, Berkeley, Berkeley, CA 94720

AND

R. J. STRANGEWAY AND P. L. PRITCHETT
University of California, Los Angeles, Los Angeles, CA 90095
Received 1999 March 26; accepted 2000 January 26

ABSTRACT

We present a detailed description of the auroral kilometric radiation (AKR) source region based on observations from the *Fast Auroral SnapshoT* (*FAST*) satellite and discuss how these new results may pertain to solar and stellar radio sources. *FAST* satellite observations are directly within the AKR source region and have unprecedented spatial and temporal resolution. They confirm many of the fundamental elements of the electron-cyclotron maser mechanism but with substantial modification. The most important modification is that the emissions do not draw their energy from a loss-cone instability; rather, the radiation results from an unstable "horseshoe" or "shell" distribution. The most far-reaching implication is that the electron-cyclotron maser is directly associated with a particular type of charged particle acceleration, a magnetic field–aligned (parallel) electric field in a dipole magnetic field. These findings change several of the characteristics of the electron-cyclotron maser mechanism and may necessitate reanalysis of some astrophysical radio sources. Under the shell instability, radio emissions with brightness temperatures $\sim 10^{14}$ K, the steady state limit of the loss-cone instability, may be continuous. Through observations, we demonstrate that source brightness may be as high as 10^{20} K in steady state. A moderately or strongly relativistic beam may result in broadband emissions. A loss cone is not required, so the radiation source may be high above the stellar or planetary surface. Although the generation is in the X mode with $k_{||} = 0$, we suggest that the radiation, guided by a density cavity that is created by the parallel electric field, efficiently converts to the R mode, which experiences substantially lower absorption at higher harmonics. These findings also suggest that parallel electric fields may be a fundamental particle acceleration mechanism in astrophysical plasmas.

Subject headings: acceleration of particles — Earth — MHD — masers — plasmas

1. INTRODUCTION

The purpose of this article is to put recent findings on the auroral kilometric radiation (AKR) source mechanism into astrophysical context. Satellite observations within the AKR source region (Ergun et al. 1998a; Delory et al. 1998; Strangeway et al. 1998) and numerical simulations (Pritchett et al. 1999) indicate an important modification to the loss-cone electron-cyclotron maser process as put forth by Wu & Lee (1979) and Melrose & Dulk (1982). These findings may compel some astrophysical applications of the electron-cyclotron maser to be reanalyzed but also allow the electron-cyclotron maser to be applied to radio sources that have not been considered candidates in the past; for example, very bright, continuous sources or sources far above a stellar surface.

The loss-cone electron-cyclotron maser (Wu & Lee 1979; Melrose & Dulk 1982), put forth as the source of auroral kilometric radiation, has been postulated as a source for a number of radio emissions. Radio sources include planetary radiation from all of the magnetized outer planets (Zarka 1992), solar microwave spikes associated with impulsive flares (Melrose & Dulk 1992; White, Melrose, & Dulk 1983; Benz, Bernold, & Dennis 1983; Willson 1985), solar type V radio emissions (Winglee & Dulk 1986), radio emissions from binary systems (Slee, Haynes, & Wright 1984; Doiron & Mutel 1984; Trigilio, Leto, & Umana 1998), and narrowband emissions from dwarf M flare stars (Lang et al. 1983; Lang & Willson 1988; Stepanov et al. 1995; Abada-Simon et al. 1994).

These radio sources have in common extremely high brightness temperatures, strong circular polarization, narrow bandwidths, and strong variability. Solar microwave spikes, for example, have less than 100 ms durations, less than 5% bandwidths, and have $\sim 100\%$ circular polarization (Melrose & Dulk 1992 and references therein). The short durations imply very small source sizes and hence, very high brightness temperatures. Radio flares from binary systems have similar characteristics (Trigilio et al. 1998) as do emissions associated with dwarf M flares (Lang et al. 1983). The high brightness temperatures suggest coherent generation associated with accelerated electrons rather than incoherent thermal processes. The electron-cyclotron maser mechanism is appealing because it is considered efficient and can lead to direct amplification of circularly polarized electromagnetic radiation with narrow bandwidths or fine structure.

Application of the loss-cone electron-cyclotron maser process to stellar radio emissions was inspired by research on AKR (Gurnett 1974). AKR is known to originate on auroral field lines (Kurth, Baumback, & Gurnett 1975) in regions of depleted density in which downgoing electrons are accelerated. The waves propagate primarily in the R-X mode (Green, Gurnett, & Shawhan 1977) and show strong

[1] Currently at Department of Astrophysical and Planetary Sciences and Laboratory for Atmospheric and Space Physics, University of Colorado, Boulder, CO 80303.

temporal variations and fine spectral features. AKR is generated near the electron cyclotron frequency (f_{ce}) from the free energy of the non-Maxwellian auroral electron distribution. One of the first widely accepted growth mechanisms was a loss-cone instability under weakly relativistic treatment (Wu & Lee 1979), later expanded into the electron-cyclotron maser instability (Melrose & Dulk 1982).

The loss-cone electron-cyclotron maser, herein called the "loss-cone maser," was questioned as the source of AKR by the results of two-dimensional particle simulations based on measured electron distributions (Pritchett 1984a; Pritchett & Strangeway 1985). Pritchett (1984b) suggested that a "shell distribution" (Winglee & Pritchett 1986) produced by a parallel electric field could produce strong cyclotron emissions (herein called the "shell maser"). Later, a study based on *Viking* satellite observations suggested that the free energy for AKR wave growth comes from electron distributions with $df/dv_\perp > 0$ and found the loss-cone insufficient to produce AKR (Louarn et al. 1990).

In this article, we present electromagnetic field and charged particle observations within the AKR source region (Ergun et al. 1998a; Delory et al. 1998; Strangeway et al. 1998). We show compelling evidence that the weakly relativistic electron-cyclotron maser instability is responsible for AKR and that wave emissions are from coherent generation by a "shell" instability that results from electron acceleration by a parallel electric field in a dipole magnetic field. The waves draw their energy from positive $df/dv_\perp$. The source region emissions are narrow banded ($\delta\omega/\omega < 1\%$) and, within experimental error, almost entirely in the X mode. In the source region, the wave frequency (ω) is less than the cold electron cyclotron frequency ($\omega_{ce} = e\boldsymbol{B}_0/m_e c$, where e is the fundamental charge, $\boldsymbol{B}_0$ is the ambient magnetic field, m_e is the electron mass, and c is the speed of light). Furthermore, we show that the electromagnetic wave observations within the source region are inconsistent with a loss-cone instability. These conclusions are supported by recent two-dimensional simulation results (Pritchett et al. 1999) that demonstrate that a loss-cone instability is considerably weaker than the shell instability.

These observational and numerical results may inspire reinvestigation of astrophysical radio sources that have been attributed to the loss-cone maser. The shell maser, however, results with emissions with only minor differences from those predicted by the loss-cone maser. Shell and loss-cone maser emissions are both circularly polarized emissions near ω_{ce}, have very narrow bandwidths, and can result with extremely high brightness temperatures. The differences are nearly impossible to distinguish from remote observations. For example, the shell maser emissions are slightly below ω_{ce}, while the loss-cone maser emissions are above ω_{ce}, which is identifiable only within the source region. The shell instability, however, appears more feasible because it (1) is now proved as the source of terrestrial radiation, (2) is a more powerful source, and (3) is directly associated with particle acceleration.

There are, however, several characteristics in radio emissions that can come from the shell maser but not from the loss-cone maser: very bright ($>10^{14}$ K), continuous emissions, broadband emissions, and emissions from high above a stellar surface. The loss-cone masers are expected to saturate rapidly, while a shell maser can produce either continuous or bursty emissions, depending on the electron acceleration. Loss-cone masers are confined to be near the stellar surface, whereas a shell maser may be high above the stellar or planetary surface. Under moderately relativistic acceleration ($\gamma \sim 2$), the emissions can be broadbanded.

Finally, we show examples in which AKR, generated in the X mode, efficiently converts to the R mode with a complex beaming pattern. This conversion process may be very important to stellar radio sources. A major problem of the electron-cyclotron maser mechanism is that X-mode emissions are expected to be nearly entirely absorbed as they propagate through regions in which they are at higher harmonics of the local electron gyrofrequency (Melrose & Dulk 1992). We put forth that stellar radiation, guided by a density cavity that is created by the parallel electric field, can be very efficiently converted to the R mode, which experiences substantially lower absorption at higher harmonics.

2. AKR SOURCE REGION OBSERVATIONS

2.1. *The Auroral Acceleration Region*

Auroral zone observations are well established (Carlson, Pfaff, & Watzin 1998a and references therein), so we give only a brief overview of the AKR source region. *Fast Auroral SnapshoT* (*FAST*) satellite observations in the upward current region of the auroral zone have provided conclusive evidence of charged particle acceleration by quasi-static, parallel electric fields (Carlson et al. 1998b; Ergun et al. 1998b; McFadden et al. 1998). The anti-Earthward–directed electric fields accelerate electrons Earthward that form visible auroral arcs and accelerate ion beams anti-Earthward. A simple model (similar to that in Carlson et al. 1998a) of the auroral zone is displayed in Figure 1. The auroral zone is bounded at high altitude by hot ($T_e \sim 0.5$ keV), tenuous ($n_e \sim 1$ cm^{-3}) magnetospheric plasma and at low altitude by cold ($T_e \sim 0.2$ eV), more dense ($n_e \sim 10^3$–10^5 cm^{-3}) ionospheric plasma.

The solid lines in Figure 1 represent equipotential contours that depict a parallel electric field in the auroral acceleration region. The anti-Earthward parallel electric field accelerates electrons Earthward and creates an anti-Earthward ion beam. The Earth's dipole magnetic field (*dashed lines*) plays an important role. The precipitating electrons adiabatically evolve to higher pitch angles, some mirroring, as they travel into a stronger magnetic field. The anti-Earthward ion beam experiences the opposite effect, focusing into a field-aligned beam. AKR is seen as enhanced wave emissions near the local electron-cyclotron frequency coming from this region (Bahnsen et al. 1987; Roux et al. 1993).

2.2. *Source Region Observations*

The observations that we display are from the *FAST* satellite. The instruments are described in several articles (Carlson et al. 1998a and references therein). These observations, made at unprecedented time and spatial resolution, include the first digital waveform capture in the AKR source region. The 0.5 μs resolution data had three axes of electric field ($\Delta\boldsymbol{E}$) and one axis of magnetic field ($\Delta\boldsymbol{B}$).

Figure 2 shows plasma observations within the AKR source region. The horizontal axis represents 16 s ($\sim$100 km) of the auroral zone at $\sim$4000 km altitude. The satellite was moving from south to north (see Fig. 1). The top panel (Fig. 2*a*) displays the electron energy flux as a function of energy. Darkness of shade indicates increased electron

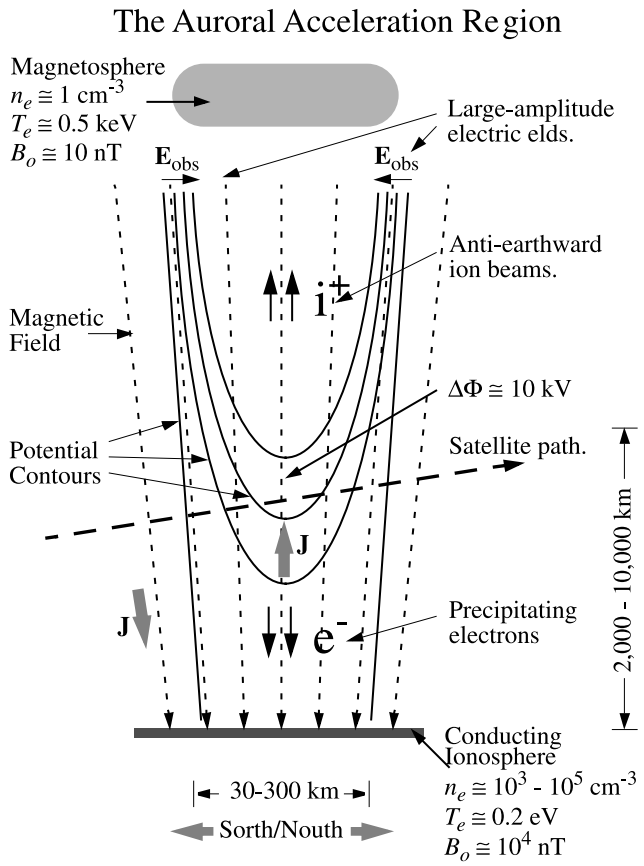

FIG. 1.—Model of the potential structure of the upward current region of the aurora. The auroral zone is bounded by hot magnetospheric plasma at high altitude and cold ionospheric plasma at low altitude. The solid lines represent equipotential contours. The dashed lines represent the ambient magnetic field. The potential contours form a parallel electric field. A satellite passing through the acceleration region (*long-dashed line*) observes precipitating electrons, anti-Earthward ion fluxes, and large-amplitude electric fields at the boundaries.

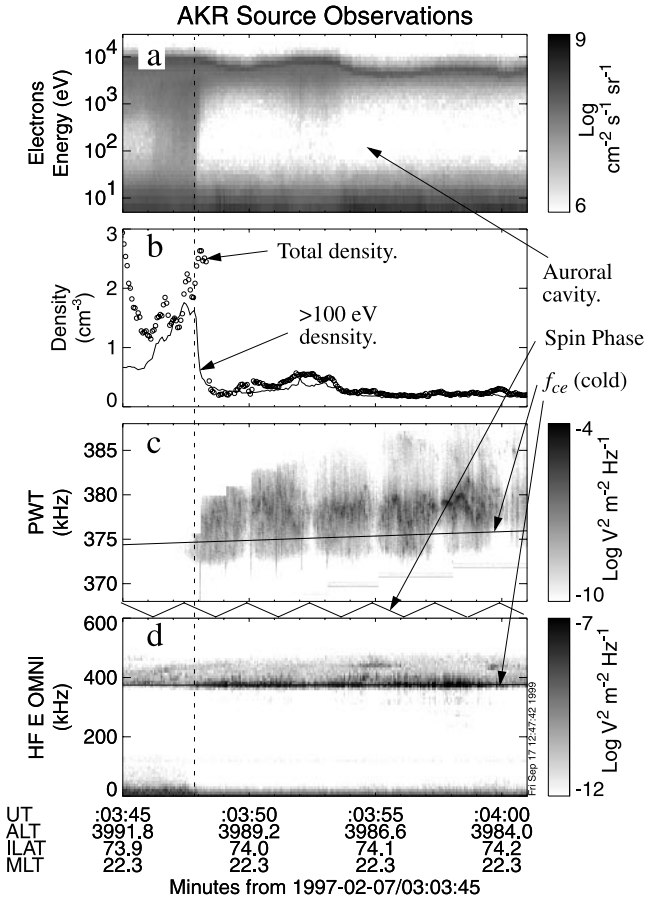

FIG. 2.—AKR source region. (*a*) Electron energy flux vs. energy and time. There are no measurable electron fluxes between ~100 eV and ~1 keV in the auroral cavity. The fluxes below ~100 eV are spacecraft photoelectrons. (*b*) The total electron density (*circles*) derived from fits to the whistler-Langmuir dispersion. The solid line is the hot (>100 eV) electron density. (*c*) Wave power as measured by the Plasma Wave Tracker. The white line is f_{ce} (±400 Hz). These data have spin modulations. The PWT covers a ~16 kHz band, the center frequency updated every 1 s. The emissions extend below f_{ce}. (*d*) High-frequency electric field power. The white line is f_{ce}.

energy flux. One can see a clear peak at ~10 keV near the beginning of the plot, decreasing to ~4 keV by the end of the plot. The electron fluxes were relatively evenly distributed in pitch angle (not displayed) except for a loss-cone at 180° (anti-Earthward). The net motion of the electrons was therefore Earthward. These precipitating electrons created visible auroral arcs.

From ~03:03:48 UT on, marked by the vertical dashed line, there were almost no detectable electron fluxes between ~100 eV and ~1 keV. At that time, the spacecraft was within the auroral acceleration region often referred to as the "auroral cavity" (e.g., Carlson et al. 1998a). Figure 2*b* displays the results of two separate methods of determining the electron density. The solid trace is the density of greater than 100 eV electrons derived from the electron fluxes (Fig. 2*a*) that were measured by an electrostatic analyzer. We call this quantity the "hot" electron density. The derived density has approximately ±25% uncertainty. The lower energy (<100 eV) electron fluxes were not included because they were dominated by spacecraft photoelectrons.

The circles in Figure 2*b* denote the density derived from fits of the electric field wave observations, representing the total density (Ergun et al. 1998a; Strangeway et al. 1998). Only fits that had better than ~±50% uncertainty are plotted. One can see that, outside of the auroral cavity, the hot and the total densities differed, indicating a substantial "cold" (<100 eV) electron population. Inside the cavity, however, the two measurements agree within expected error. These observations imply that the dominant plasma constituents were the precipitating electrons and an anti-Earthward ion beam (Ergun et al. 1998a; Strangeway et al. 1998).

Figures 2*c* and 2*d* show the electric field spectral power density as a function of frequency and time. Figure 2*d* displays the frequency span from 0 to 600 kHz at 15 kHz bandwidth. The wave power in this panel was derived from two orthogonal antennas in the spin plane and therefore shows little modulation at the spacecraft spin frequency. The dark line is f_{ce} with no relativistic correction, called the "cold" electron cyclotron frequency. Figure 2*c* displays Plasma Wave Tracker (PWT) data, which has fine frequency resolution over a limited bandwidth that encompasses f_{ce}. The frequency axis is from 368 to 388 kHz with 32 Hz resolution. The PWT has better than 50 Hz frequency stability. The dark line is the cold electron cyclotron frequency (f_{ce}). The PWT spectral power density was derived from a single antenna in the spacecraft spin plane

and therefore shows strong spin modulation. The spacecraft spin period was 5 s. The modulation is seen with a period of 2.5 s. This modulation indicates that the wave electric field was polarized perpendicular to the ambient magnetic field (Ergun et al. 1998a).

The wave emissions near f_{ce} ($\sim$375 kHz) and within the density cavity intensified by $\sim$3 orders of magnitude relative to the surrounding region (Fig. 2*d*) and clearly penetrated below f_{ce} (Fig. 2*c*). This density cavity is an AKR source region. The source region is characterized by (1) greatly increased power near f_{ce}, (2) wave emissions below f_{ce}, (3) decreased plasma density, (4) an absence of low-energy electrons fluxes, and (5) an ion beam (not displayed). Criterion (2) is more restrictive than previously published criteria (Bahnsen et al. 1987; Roux et al. 1993; Ergun et al. 1998a).

2.3. *Electron Distributions*

Figure 3*a* displays a two-dimensional electron distribution at a time of strong wave emissions below f_{ce}. The horizontal axis is the parallel (to $\boldsymbol{B}_0$) velocity; the vertical axis is the perpendicular velocity. Darkness of shade indicates increased phase space density. The region below 1 keV is not displayed since the data between 100 eV and $\sim$1 keV were at the one count level and therefore are not statistically significant, and below 100 eV, the fluxes were dominated by photoelectrons. There is a statistically significant peak in the electron distribution at $\sim$4 keV ($\sim$3.5 km s^{-1}) that is clearly visible in Figure 3*a*. The electrons have a shell-like distribution with a loss cone, also called a "horseshoe distribution."

There are two interesting properties of shell or horseshoe distributions. All of the electrons have approximately the same energy, given that the energy from acceleration ξ_Φ is greater than the source temperature ($T_e^{\rm src}$). The effective mass (γm_e) and therefore the relativistically corrected gyrofrequency ($\omega_{\rm cr} = \omega_{\rm ce}/\gamma$) of all electrons are nearly identical. The real part of the dispersion thus can be analyzed simply with "heavy" electrons. Since the plasma frequency ($\omega_{\rm pe}$) is much smaller than $\omega_{\rm cr}$, the right cutoff becomes

$$\omega_{\rm right} \cong \omega_{\rm cr} + 2\omega_{\rm pe}^2/\omega_{\rm cr} \, . \qquad (1)$$

In the auroral density cavity, $\omega_{\rm right}$ is generally less than $\omega_{\rm ce}$, so the *R*-*X* mode can propagate below $\omega_{\rm ce}$.

The growth rate for the electron-cyclotron maser is derived by integrating $df/dv_\perp$ over a surface defined by the resonance condition (Melrose & Dulk 1982):

$$\omega - s\omega_{\rm ce}/\gamma = k_{||} v_{||}, \; s = 0, +1, +2 \ldots \, . \qquad (2)$$

A positive slope, $df/dv_\perp > 0$ or $df/dv_{||} > 0$, is seen at all pitch angles except in the region of the loss cone (Fig. 3*a*). There is also a statistically significant, but much weaker, $df/dv_\perp > 0$ in the loss cone.

Two integration surfaces for the electron-cyclotron maser ($s = 1$) are drawn on Figure 3*a* (*dashed lines*). Contour 1 displays the integration surface of the loss-cone instability. To optimize wave growth, the loss-cone contour requires a wave frequency $\sim$1.5 kHz *above* the f_{ce} and a finite $k_{||}$ ($\sim -1 \times 10^{-3}$ m^{-1}). Contour 2, the integration surface of the shell instability, requires a wave frequency $\sim$2.75 kHz *below* f_{ce} and $k_{||} = 0$. The distribution shows evidence of wave growth from both the loss-cone and the shell instability. The loss cone is filled in, and the growth rate is near zero. The perpendicular electron distribution has a broader

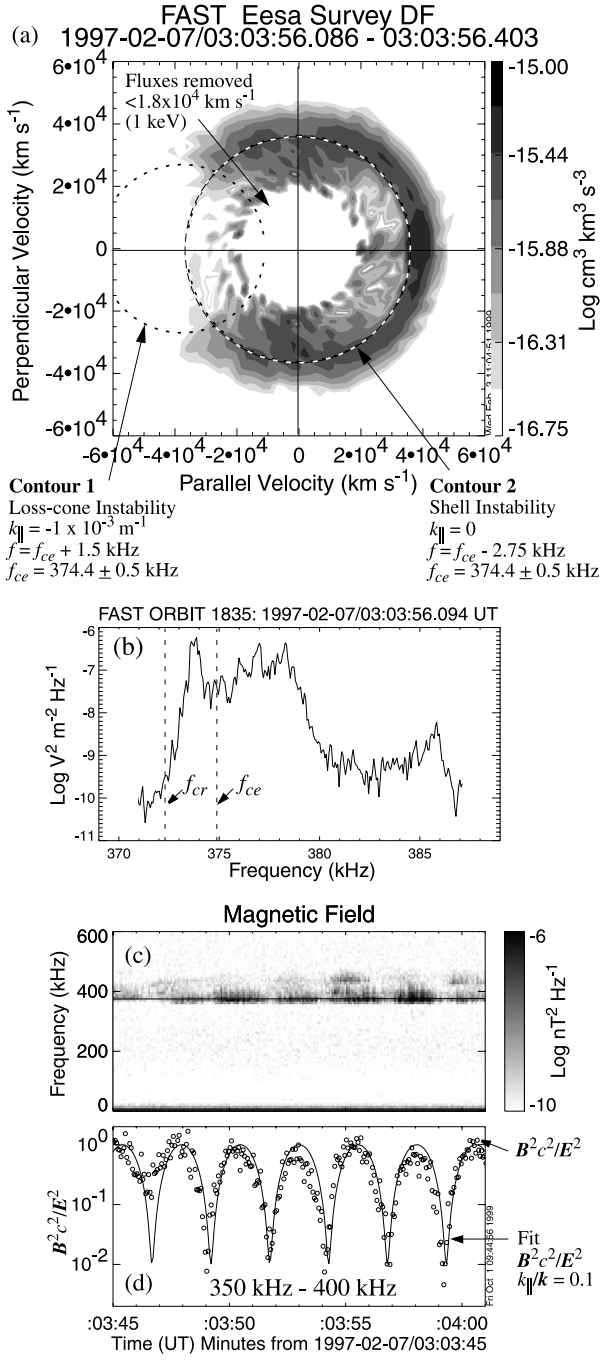

FIG. 3.—(*a*) Two-dimensional electron distribution in the AKR source region. Darkness of shade indicates increased phase-space density. Electrons less than 1 keV have been removed. One can see a clear horseshoe shape in distribution, which forms a partially open shell in three dimensions. The dashed lines represent integration surfaces to calculate wave growth. Contour 1 is optimized for the loss-cone maser, contour 2 for the shell maser. (*b*) The wave power vs. frequency taken within the interval that the distribution in the top panel was compiled. The peak is between f_{cr} and f_{ce}. (*c*) The magnetic spectral power density. These data are from a single search coil in the satellite spin plane and therefore show strong spin modulation. The timescale is the same as that of Fig. 2. (*d*) The ratio of magnetic energy density and electric energy density (*circles*). The magnetic field energy density is spin modulated, whereas the electric field energy density is from two antennas and therefore not modulated by spin. The solid line is the predicted ratio if $k_{||}/k = 0.1$, the limit of uncertainty in the measurement. The uncertainty in the magnetic field polarization comes primarily from the compilation time of the frequency vs. time spectrogram (64 ms). In that time, the satellite (5 s period) rotates 4°.6. Electrostatic pick up at $\sim$400 kHz, can account for 2% (1°) uncertainty. The data indicate that the wave magnetic field is within $\sim$6° of the ambient magnetic field.

peak giving evidence of diffusion in velocity space to lower energies.

Similar distributions have been analyzed in detail by Pritchett et al. (1999) with two-dimensional electromagnetic particle simulations. They conclude that (1) the $k_{||} = 0$ amplification (shell maser) is substantially stronger than amplification from loss-cone maser ($k_{||} \neq 0$) and (2) the electron distributions observed by *FAST* are consistent with the shell maser; the observed velocity-space diffusion at $\sim 90^\circ$ pitch angles cannot be produced by a loss-cone maser.

2.4. *Wave Characteristics*

Simulations and analytic calculations using the high-resolution particle data suggest the shell mazer should dominate AKR wave growth. We test this prediction through close examination of wave data. Under the shell mazer, the emitted waves should be below f_{ce} and, since $k_{||} = 0$, purely in the X mode. Under the loss-cone maser, the emissions should be above f_{ce} and should have a substantial R-mode component ($k_{||}/k_{\perp} \sim 0.2$).

Figure 3*b* shows a slice of the PWT data (from Fig. 2*c*). These data were taken at the same time that the distribution in Figure 3*a* was compiled. The vertical axis is spectral power density, and the horizontal axis is frequency, focusing on a narrow band about f_{ce}. The wave power has a clear peak between the relativistically corrected electron cyclotron frequency (f_{cr}) and the cold electron cyclotron frequency (f_{ce}).

The position of the peak below f_{ce} is consistent with wave growth from the shell instability slightly below (in altitude) the satellite but is difficult to explain with the loss-cone instability. If waves are generated at a lower altitude (below the spacecraft), they are free to propagate to higher altitudes; thus the source of emissions above f_{ce} is ambiguous. We cannot immediately distinguish if they are generated locally or at a lower altitude.

Waves generated by the loss-cone instability, however, have a finite (negative) $k_{||}$ and should be propagating, as generated, obliquely but to higher altitudes. To observe the emissions below f_{ce}, these waves would have to be reflected. It is very unlikely that a density boundary could be sustained on a field line within the auroral cavity, but it is possible that loss-cone–generated waves could reflect from irregular perpendicular boundaries of the density cavity and emerge with a downward propagation velocity. So generation of waves below f_{ce} by the loss-cone instability, however unlikely, cannot be ruled out completely.

Wave polarization provides the most convincing evidence of the growth mechanism. Under the shell instability, the waves in the source region should be purely in the X mode. The wave electric field ($\Delta \boldsymbol{E}$) has been demonstrated to be purely perpendicular to $\boldsymbol{B}_0$ within experimental uncertainty ($\pm 4^\circ$; Ergun et al. 1998a). The amplitude modulation in Figure 2*c* (also in Fig. 4*c*) attests to this conclusion. This finding confirmed that the waves were generated in the R-X mode, not the L-O mode.

Here, we examine the polarization of the wave magnetic field ($\Delta \boldsymbol{B}$). Under the shell instability, AKR is in the X mode, so $\Delta \boldsymbol{B}$ should be purely parallel to $\boldsymbol{B}_0$. The loss-cone instability predicts $|k_{||}/k| \cong 0.13$ (see Fig. 3*a*), in which case $\Delta \boldsymbol{B}$ should have a measurable perpendicular component. Figures 3*c* and 3*d* detail the magnetic field wave polarization. Figure 3*c* shows the magnetic spectral power density. The dark line is f_{ce}. The magnetic field at AKR frequencies is measured with a single search coil and therefore is modulated at twice the spacecraft spin period with a phase that indicates that $\Delta \boldsymbol{B}$ is very near to $\boldsymbol{B}_0$. The electric field energy density (presented earlier in Fig. 2*d*) is derived from two orthogonal antennas in the spin plane and shows little modulation due to spacecraft rotation.

The measured ratio of the magnetic to electric energy density ($\boldsymbol{B}^2c^2/\boldsymbol{E}^2$) is plotted in Figure 3*d* as circles. Superimposed on the plot is a fit of $\boldsymbol{B}^2c^2/\boldsymbol{E}^2$ with $|k_{||}/\boldsymbol{k}| = 0.1$ (6°). This ratio is at the measurement uncertainty, given at the power level on the right of the plot. On the far left, there is not enough power to determine the polarization accurately.

Figure 3*d* demonstrates that the polarization angle of $\Delta \boldsymbol{B}$ was less than 6° from parallel to $\boldsymbol{B}_0$ and inconsistent with the loss-cone instability, which should produce a slightly larger polarization angle. Furthermore, as discussed above, loss-cone–produced emissions would have to reflect and scatter to reach lower altitudes so that $f < f_{ce}$, once again inconsistent with such a confined polarization. We interpret these data as compelling evidence that the AKR emissions are generated from a shell maser rather than the loss-cone maser.

2.5. *Source Region 2*

In the above example, the expected ratio $|k_{||}/k|$ was small and near the uncertainty of the measurement, so we examine an orbit that has a much larger expected deviation. Figure 4 shows a second AKR source region from another orbit. The format is the same as in Figure 2, and the observations in Figure 4 have many of the same properties as those in Figure 2. There were monoenergetic, precipitating electron fluxes throughout. In the density cavity (left border until 21:02:15 UT), there were field-aligned, anti-Earthward ion fluxes (not displayed) and decreased electron fluxes below ~ 1 keV. The hot electron density (> 100 eV) agrees with that derived from the wave dispersion indicating that there was no cold population. The wave emissions near f_{ce} intensified and were seen below f_{ce}.

The left-hand side of Figure 4 is an AKR source region. AKR is very intense, greater than 10^{-4} V m^{-2} Hz^{-1} as seen in the PWT (Fig. 4*c*) and the HF wave data (Fig. 4*d*). At the right edge of the density cavity ($\sim$21:02:14.5 UT), there was a sudden shift in the PWT band caused by an on-board error determining f_{ce}. The magnetic tracking recovers enough by 21:02:20 UT to see that there was significantly lower power near f_{ce} outside of the density cavity.

Figure 5*a* displays a two-dimensional electron distribution. The electron distribution has similar characteristics to those in Figure 3*a*, except the energies are higher. There are two contours displayed in this figure. Contour 1 ($f = f_{ce} + 5.0$ kHz, $k_{||} = -2.3 \times 10^{-3}$ m^{-1}) is a loss-cone integration surface ~ 5 kHz above f_{ce}. One can see that, under the loss-cone instability, frequencies between f_{ce} and $f_{ce} + 10$ kHz should have $k_{||}$ on average $\sim 2.3 \times 10^{-3}$ m^{-1}, or $|k_{||}/k| \cong 0.3$.

Figure 5 displays the magnetic field polarization in the same fashion as in Figure 3. Figure 5*b* displays the wave spectral power density versus frequency. Again, there were strong emissions below f_{ce}. Figure 5*c* shows the magnetic field spectral power density as a function of frequency and time. One can see a strong modulation in power at twice the spacecraft spin frequency. The peaks in power occur when the search coil is nearly aligned with $\boldsymbol{B}_0$, the troughs occur

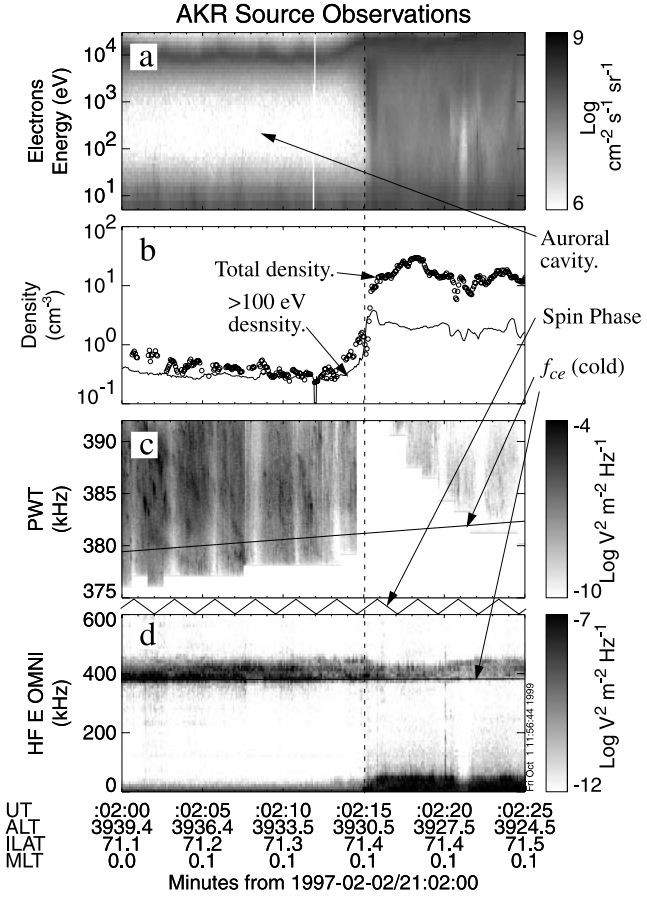

FIG. 4.—AKR source region. This figure is in the same format as Fig. 2. (*a*) Electron energy flux vs. energy and time. There are no measurable electron fluxes between ~100 eV and ~1 keV in the auroral cavity. The fluxes below ~100 eV are spacecraft photoelectrons. (*b*) The total electron density (*circles*) derived from fits to the whistler-Langmuir dispersion. The solid line is the hot (>100 eV) electron density. (*c*) Wave power as measured by the Plasma Wave Tracker. The white line is f_{ce} (±400 Hz). These data have spin modulations. The PWT covers a ~16 kHz band, the center frequency updated every 1 s. The emissions extend below the cold electron cyclotron frequency. (*d*) High-frequency electric field power. The white line is f_{ce}.

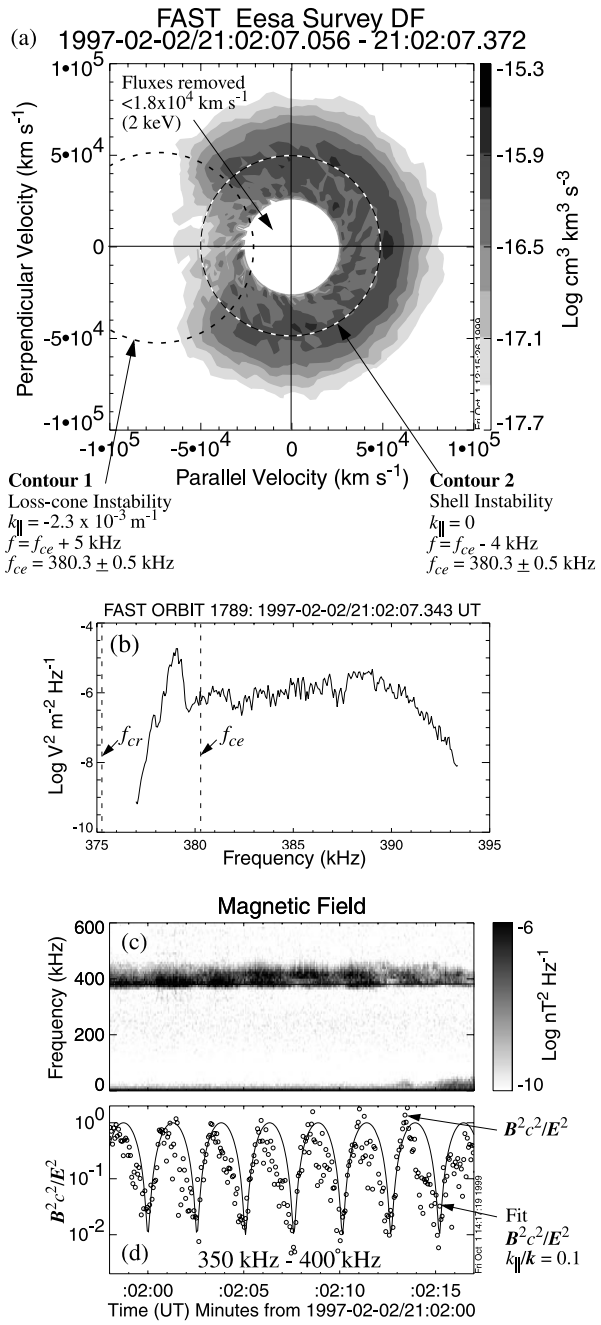

FIG. 5.—Two-dimensional electron distribution in the AKR source region. Darkness of shade indicates increased phase-space density. Electrons less than 3 keV have been removed. One can see a clear horseshoe shape in distribution, which forms a partially open shell in three dimensions. The dashed lines represent integration surfaces to calculate wave growth. Contour 1 represents the integration surface of the loss-cone maser; contour 2 is for the shell maser. There is erosion at oblique pitch angles. (*b*) The wave power vs. frequency taken within the interval that the distribution in the top panel was compiled. The peak is between f_{cr} and f_{ce}. (*c*) The magnetic spectral power density. These data are from a single search coil in the satellite spin plane and therefore show strong spin modulation. The timescale is the same as that of Fig. 3. (*d*) The ratio of magnetic energy density and electric energy density (*circles*). The magnetic field energy density is spin modulated, whereas the electric field energy density is from two antennas and therefore not modulated by spin. The solid line is the predicted ratio if $k_{||}/k = 0.1$, the limit of uncertainty in the measurement. The uncertainty in the magnetic field polarization comes primarily from the compilation time of the frequency versus time spectrogram (64 ms). In that time, the satellite (5 s period) rotates 4°.6. Electrostatic pick up at ~400 kHz, can account for 2% (1°) uncertainty. The data indicate that the wave magnetic field is within ~6° of the ambient magnetic field.

when the search coil is normal to $\boldsymbol{B}_0$. Figure 5*d* plots the measured ratio $\boldsymbol{B}^2c^2/\boldsymbol{E}^2$ and a fit of $\boldsymbol{B}^2c^2/\boldsymbol{E}^2$ with $|k_{||}/k| = 0.1$, the uncertainty of the measurement. These data clearly are inconsistent with the loss cone instability that predicts $|k_{||}/k| \cong 0.3$; the minima in the ratio $\boldsymbol{B}^2c^2/\boldsymbol{E}^2$ would be an order of magnitude less deep.

Twenty-five source region crossings from 1997 January through 1997 March were examined in this study. All of the source region observations had the polarization of $\Delta\boldsymbol{B}$ within 6° of $\boldsymbol{B}_0$ in the frequency range within 10 kHz of f_{ce}. In other words, the polarization of the magnetic field is consistent with wave generation purely in the *X* mode with $k_{||} = 0$. In many examples, the polarization was inconsistent with loss-cone growth. *FAST* source region observations provide compelling evidence that AKR is generated by an electron-cyclotron maser with a shell instability. The loss cone does not appear to play a major role.

2.6. *Conversion to the R Mode*

Although source region observations show that AKR is generated as *X*-mode emissions, remote observations of the

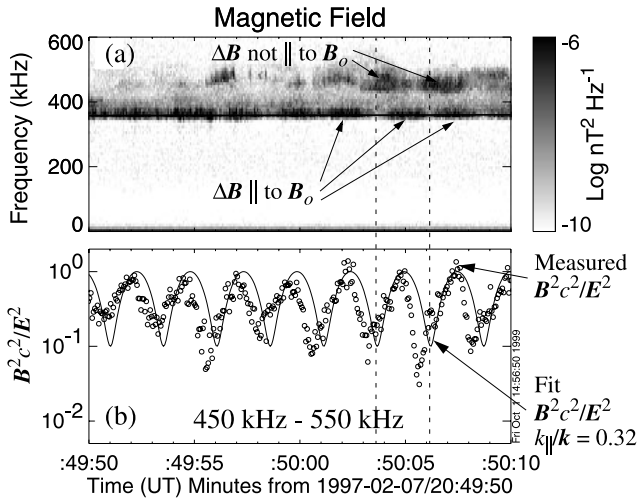

FIG. 6.—(*a*) Magnetic spectral power density. These data are from a single search coil in the satellite spin plane and therefore show strong spin modulation. (*b*) The ratio of magnetic energy density and electric energy density (*circles*). The magnetic field energy density is spin modulated, whereas the electric field energy density is from two antennas and therefore not modulated by spin. The solid line is the predicted ratio if $k_{||}/k = 0.1$. The phase shift indicates that the wave magnetic field is polarized at $\sim 45°$ of the ambient magnetic field. These emissions are in the *R-X* mode.

escaping radiation indicates a significant conversion to the *R* mode. This conversion is demonstrated in Figure 6. Figure 6*a* shows an overview of the magnetic field spectral power density. The most interesting aspect of these data is that the nulls in power at frequencies ~ 100 kHz above f_{ce} (e.g., ~ 500 kHz) do not occur at the same time as those near f_{ce}. Figure 6*b* compares the spin-modulated $\Delta \boldsymbol{B}$ with the $\Delta \boldsymbol{E}$ (derived from a vector measurement) in the frequency band from 450 to 550 kHz, well above f_{ce}; the AKR was generated at an altitude considerably below the spacecraft. The nulls of these free-space emissions (Fig. 6*b*) are not as deep as in the source region and, interestingly, are offset by $\sim 45°$ in spin phase. These observations have a unique interpretation. The emissions are in the *R-X* mode and linearly polarized at $\sim 45°$ from $\boldsymbol{B}_0$. The depth of the nulls indicates that the angular width of $k \sim \pm 10°$. These emissions were "beamed" to the spacecraft from a small source below and ahead of the spacecraft at $\sim 45°$ angle.

The amplitude of the emissions reaches nearly 10^{-8} W m^{-2} Hz^{-1} and is almost as intense as the nearby source region emissions. From the frequency of the emissions and the polarization angle, we can estimate the distance to the source is ~ 1100 km, and the size of the source is ~ 350 km. The source region energy density thus must have exceeded $\sim 10^{-15}$ J m^{-3}, which would be among the most intense sources that we have observed. The source brightness temperature exceeds 10^{20} K, a level that cannot be reached by the loss-cone maser continuously. Apparently, the conversion to the *R-X* mode must have been extremely efficient. This highly efficient conversion to *R-X* mode from the generation in the *X* mode appears in many of the examined cases.

3. DISCUSSION

The high-resolution observations of electron distributions and electromagnetic waves within the AKR source region allow us to resolve the properties of electron-cyclotron maser instability. Since the theory of electron-cyclotron masers is well developed, we concentrate of the differences between the shell maser and loss-cone maser.

3.1. *Formation of Shell Distributions, Saturation*

An important difference between the shell maser and the loss-cone maser is the saturation of wave growth. Under the loss-cone maser, the radiation process causes diffusion in velocity space that fills the loss cone and can ultimately "quench" the instability (Melrose & Dulk 1982). The loss-cone maser can not sustain a high brightness temperature ($>10^{14}$ K) in steady state. Brighter emissions are possible for pulses.

The shell instability has continuous pumping of free energy into the maser from the parallel electric field. The AKR simulations (Pritchett et al. 1999) show that, under steady state particle acceleration, very strong emissions can be steady state. Observations support this conclusion and indicate that the shell maser can sustain brightness temperatures as high as $\sim 10^{20}$ K in steady state.

The formation of the shell distribution is discussed by Chiu & Schulz (1978). The source electrons are energized by the parallel electric field into an increasing magnetic field, then adiabatically evolve to higher pitch angles forming the shell distribution. The acceleration and evolution can be continuous or occur in discrete steps (Winglee & Pritchett 1986). The magnetic mirror ratio (R_M) for adiabatic evolution to $\sim 90°$ pitch angle needs to be greater than $\xi_\Phi / T_e^{\rm src}$, the ratio of the acceleration energy to the source temperature. In the auroral zone, this ratio is greater than 10.

Wave growth causes electrons at $\sim 90°$ pitch angles diffuse (in velocity space) to lower energy. This perpendicular diffusion is observed in the source region distributions (Figs. 3*a* and 5*a*) and is considered strong evidence of the shell instability. The diffused electrons can be removed by the parallel electric field or, depending on the distribution of the parallel electric field, can be trapped. The trapped electrons do not always appear in auroral source regions. Maser radiation can continue to grow from the $df/dv_\perp > 0$ caused by the trapped population (discussed in detail by Louarn et al. 1990). Thus, the shell maser can sustain high brightness temperatures in steady state, as long as the acceleration is maintained. Emissions may be bursty if the particle acceleration is impulsive or bursty.

3.2. *Parallel Electric Fields*

An important implication of the above observations is that one of the most powerful known radio emission processes is associated with a particular type of charged particle acceleration, a parallel electric field in a dipole magnetic field. Although one cannot conclude that shell distributions are created uniquely by parallel electric fields, they are nearly impossible to create under any other currently known acceleration mechanism. The parallel electric fields set up the necessary conditions for direct amplification of electromagnetic waves and their subsequent escape.

There are two principal conditions for direct amplification of electomagnetic waves under the electron-cyclotron maser (Wu & Lee 1979). The unstable distribution need be created; the electron-cyclotron maser requires $df/dv_\perp > 0$. Also required is a low plasma density such that $\omega_{pe} \ll \omega_{ce}$. Mathematically, the second requirement, combined with relativistic correction, creates a topological change to the integration surfaces that determine the growth rate that

allows the wave growth to occur (Wu & Lee 1979). Although a loss cone can satisfy the first requirement (unstable distribution), it does not necessarily satisfy the second ($\omega_{pe} \ll \omega_{ce}$) whereas the parallel electric fields, as a minimum those in the auroral zone, appear to satisfy both conditions at once. Ironically, Wu & Lee (1979) surmised that a parallel electric field created the low-density cavity.

The shell distribution also alters the real part of the dispersion. As pointed out above, the electron mass is uniformly increased, so the relativistically corrected electron cyclotron frequency (ω_{cr}) is decreased. The effective temperature of the plasma, although clearly non-Maxwellian, is also increased to $\sim \xi_\Phi$. For a wave growth with $k_{||} = 0$, the right cutoff must be less than the cold cyclotron frequency ($\omega_{right} < \omega_{ce}$). This basic condition is satisfied if

$$\xi_\Phi / m_e c^2 > 2\omega_{pe}^2/\omega_{cr}^2, \quad \text{where } \omega_{cr} \gg \omega_{pe} . \tag{3}$$

The above formula represents a necessary condition for the shell maser.

3.3. *Bandwidth*

An often mentioned characteristic of the electron-cyclotron maser is that the emissions are expected to have narrow bandwidths or fine structure. Fine structure in auroral emissions consists of falling or rising tones at less than 1% bandwidth (Figs. 2*c* and 4*c*). Under the shell instability, the bandwidth or fine structure is grossly restricted to $(\omega_{ce} - \omega_{cr})/\omega_{ce}$, e.g., $\Delta\omega/\omega_{ce} < (\gamma - 1)/\gamma$. Electron energies in the auroral region rarely exceed ~ 30 keV and are typically ~ 10 keV, so the observed narrow bandwidths of AKR are not surprising. Moderately relativistic acceleration combined with a high source temperature can produce much larger bandwidths. Interestingly, the emission frequencies also can be significantly below f_{ce}.

3.4. *Convective Growth*

The convective growth limitation has been one of the more controversial aspects of the loss-cone–driven electron-cyclotron maser (Omidi & Gurnett 1982). We demonstrate this controversy with the examples given in this paper. Under linear theory, a ray is amplified by a factor $e^{\beta\tau}$, where β is the absolute growth rate. The time (τ) that the ray can experience amplification is critical. In the above examples, the loss-cone maser in the auroral zone predicts an oblique group velocity with a component parallel to $\boldsymbol{B}_0$ of $\sim 0.1c$. The motion along $\boldsymbol{B}_0$ causes the ray to go out of resonance (e.g., eq. [1]) with the maser since the ambient electron cyclotron frequency changes. The observed bandwidths of AKR are ~ 1 kHz, so we roughly estimate that a change in f_{ce} of 1 kHz will arrest growth. Such a change occurs in ~ 8 km, limiting τ to ~ 0.3 ms. This implies an unphysical result that growth rates would have to exceed the wave bandwidth for significant amplification to occur. Such large growth rates also are not directly supported by observed distributions.

The shell maser, on the other hand, does not suffer such a strong limitation. The ray paths are perpendicular to $\boldsymbol{B}_0$ and, to lowest order, do not see a change in f_{ce} nor suffer a convective growth limitation.

3.5. *Escaping Radiation*

A major difficulty in applying the cyclotron maser to stellar radio sources and, in particular, solar microwave bursts is that fundamental emissions are expected to be nearly entirely absorbed as they propagate through regions in which they are at higher harmonics of the local electron gyrofrequency (Melrose & Dulk 1992). There are several possible windows of escape: nearly parallel propagation (*R* mode), where the optical depth is small, nearly perpendicular propagation with partial mode conversion, or mode conversion and other nonlinear processes in or near the absorption layer (Robinson 1989). Since the optical depth at the second harmonic absorption layer for AKR or planetary radiation is small, one cannot directly observe a mechanism that would apply to stellar sources. However, the AKR observations may shed some light onto a possible solution.

The AKR source region is in a density cavity bounded by a region containing a much denser (a factor of 2–100) thermal population (Fig. 7). The source region emissions, generated in the *X* mode, propagate normal to the magnetic field and are eventually reflected at the cavity boundary. Downward-propagating emissions will also reflect owing to the increasing magnetic field. Thus, the only escape is propagation away from the stellar or planetary surface (Fig. 7). An inhomogeneous density structure in the source region will ultimately scatter the emissions to upward propagation with finite $k_{||}$. This process is simple linear refraction on the *R*-*X* branch.

The basic idea is as follows (Fig. 7). The waves, upon reflecting, scatter in angle. If the waves acquire a significant $k_{||}$, they can escape without further reflection. Otherwise, the waves experience more angular scattering. A long, narrow cavity will focus the rays into a beam. The waves

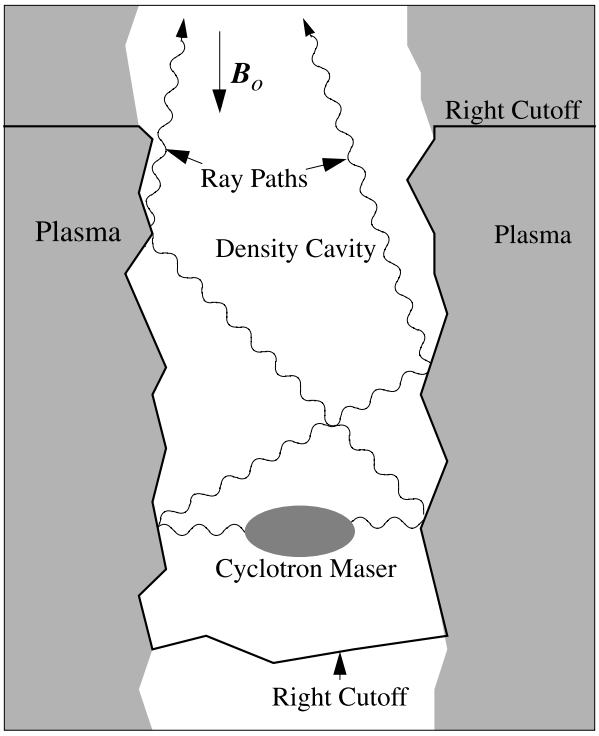

FIG. 7.—Cartoon of the electron-cyclotron maser source region. The radiation propagates at right angles as generated. The rays cannot escape the cavity until they reach weaker magnetic fields (higher altitude) and are above the right cutoff, which requires reflection at the boundaries of the cavity. The cavity can guide the waves and efficiently convert the radiation to more parallel propagating *R*-*X* mode. This process is observed for AKR.

continue to be guided in the density cavity until it reaches higher altitudes (weaker $\boldsymbol{B}_0$) at which the wave frequency exceeds the right cutoff ($f_{\rm right}$) in the plasma surrounding the cavity. At that point, the emissions can freely propagate into the surrounding medium. This process is supported by observation (Fig. 6).

In the auroral region, the wave emissions indicate a highly efficient conversion to parallel propagation (Fig. 6). We speculate that this "guiding cavity," combined with the observed inhomogeneous plasma density, favors the conversion of a substantial part of the radiation into the *R-X* mode. The physical dimensions of the auroral cavity, interestingly, are not particularly favorable for a highly efficient conversion. The perpendicular (to $\boldsymbol{B}_0$) dimension (~ 100 km) is typically larger than the parallel dimension (tens of kilometers). A deep cavity in a stellar magnetosphere, however, could result with significant power conversion to the *R* mode that suffers much less second-harmonic absorption (Holman, Eichler, & Kundu 1980).

Another difference between the loss-cone instability and shell instability is the altitude above the stellar or planetary surface of the maser. The loss-cone angle depends on the mirror ratio with respect to the *stellar surface*, often requiring the source to be close to the surface. Although a strong magnetic field near the surface will satisfy the requirement that $\omega_{\rm pe} \ll \omega_{\rm ce}$, the radiation needs to escape through a relatively dense plasma and thus will experience strong absorption at higher harmonics. The shell distribution requires a moderate mirror ratio with respect to the *point of acceleration* and can occur at any altitude above the stellar or planetary surface. The ambient plasma density can be lower, and thus harmonic absorption can be lower.

3.6. *Generation at the Second Harmonic*

Generation at the second harmonic ($s = 2$) was proposed by Melrose & Dulk (1982) to circumvent gyroharmonic absorption problem; the optical depths at $s > 2$ in stellar environments may permit escape. Melrose & Dulk (1982) also stated that growth at the second harmonic is questionable owing to the competition with the fast-growing fundamental emissions. *FAST* satellite observations, within the accuracy of the instruments (< 50 dB harmonic distortion), do not detect second-harmonic radiation in the auroral zone in any of the 25 cases examined. Radiation at the second harmonic appears to be at least several orders of magnitude less then the fundamental.

4. APPLICATION TO ASTROPHYSICAL SOURCES

The loss-cone electron-cyclotron maser instability has been suggested for several stellar sources including solar microwave bursts, radio emissions from RS CVn binary stars, and dwarf M stars (Lang 1994). All of these sources are associated with charged particle acceleration within a region of strong magnetic field. We suggest that the shell instability may be applicable to these examples and also may be applicable to longer duration sources for which the electron-cyclotron maser has not been considered viable in the past.

4.1. *Solar Microwave Spikes*

The most conspicuous of the applications of the electron-cyclotron maser has been solar microwave spikes (Melrose & Dulk 1982; White et al. 1983; Benz et al. 1983; Willson 1985). These high-frequency (~ 100 MHz to 5 GHz) radio emissions occur during solar radio flares, are 100% circularly polarized, have narrow bandwidths ($< 5\%$), appear in short bursts (< 100 ms), and have brightness temperatures in excess of 10^{12} K. These properties imply a nonthermal emission that can be accounted for by coherent amplification through the electron-cyclotron maser.

The most serious drawback in applying the electron-cyclotron maser mechanism is the expected absorption at the second harmonic. The optical depth is $\sim 10^4$ assuming $\omega_{\rm pe}/\omega_{\rm ce} \sim 0.1$. A number of possible explanations have been put forth, including growth at higher harmonics (Melrose & Dulk 1992; Willes & Robinson 1996) and escape through an *O*-mode window (Robinson 1989). Alternative growth mechanisms have also been put forth, including beam-driven free-electron maser mechanism and beam-driven cyclotron resonance (Tsui 1996).

We suggest that the shell distribution model can account for many properties of the emissions including the short bursts if the electron acceleration is transient. Furthermore, the shell model predicts a cavity ($\omega_{\rm pe}/\omega < \sim 0.01$; see eq. [3]), which, when combined with efficient conversion to $\theta \sim 0$, can greatly reduce the absorption. These emissions occur in the impulsive phase of the acceleration process, during which the cavity may penetrate to regions where the magnetic fields reach several hundred gauss.

The shell maser may also be applicable to the postimpulsive phase of the solar radio burst. These long-lived emissions last for hours and include highly circularly polarized emissions with brightness temperatures of 10^9 to 10^{12} K, properties that are well suited for the shell maser under continuous acceleration. Competing mechanisms include coherent generation from electron beams (e.g., solar type III radio emissions; Lin et al. 1986; Ergun et al. 1998c) or accelerated shock fronts (e.g., type II radio emissions; Cane et al. 1981). The competing mechanisms require conversion from plasma modes to electromagnetic radiation and further interaction with the magnetized plasma to bring about circular polarization.

The shell maser can apply to continuous emissions. Another viable candidate for the shell maser may be the meter-wavelength solar radio bursts, discussed by Lang (1994), who suggests that intense flares may provide a long-lived radio source. These long-lived (hours) emissions occur higher above the solar surface, can be highly circularly polarized, and have high brightness temperatures (up to 10^{12} K).

4.2. *Dwarf M Stars*

Short-duration (< 100 ms) radio spikes near 20 cm wavelength from dwarf M flare stars are nearly 100% circularly polarized with amplitudes in excess of 100 mJy (Lang et al. 1983). The impulsive bursts indicate a small source region, far less than the stellar diameter, and thus imply high brightness temperatures ($> 10^{15}$ K). Lang (1994) attributed these emissions to a coherent plasma process such as the electron-cyclotron maser. The electron-cyclotron maser can directly generate the circularly polarized electromagnetic emissions. Since the loss-cone maser and shell maser emissions are distinguishable only within the source region, either of the mechanisms can be considered. The more powerful shell instability, however, may be more viable as it is now proved as the source of terrestrial radiation.

We suggest that the shell-type maser is also a viable candidate to produce the quasi-periodic emissions reported

from dwarf M AD Leonis (Lang 1994). These emissions have several characteristics that make the electron-cyclotron maser an attractive candidate; they are nearly 100% circularly polarized and have very high brightness temperatures. These emissions, however, have broader bandwidth and are modulated at ~ 1 s periods. The suggested source of these modulations is modulated particle acceleration or magnetic flux tube oscillations.

Since the shell maser emissions are directly associated with particle acceleration, modulations in electron acceleration can produce amplitude modulations in the radio emissions. Modulations in AKR intensities associated with electron flux and/or energy modulations have been observed. A broad bandwidth requires a complex explanation under the electron-cyclotron maser. There are two possibilities. Radiation at multiple points along a magnetic flux tube would produce what appears to be broadband emissions to a remote observer (as in the case of AKR). Moderately relativistic ($\gamma \sim 2$) electron acceleration also can produce broadband emissions through the shell maser. As in the case of solar microwave spikes, the most viable competing mechanisms are coherent beam-plasma processes.

The shell maser also may apply to more continuous emissions from dwarf M flare stars. Extremely bright, narrowband (2%) emissions from dwarf M stars were seen to persist over many minutes to hours (Lang & Willson 1988). It was suggested that the emissions could result from the electron-cyclotron maser emission if there was persistent flaring. In this example, the shell maser appears to be applicable under persistent flaring or continuous acceleration.

4.3. *RS CVn Binaries*

Radio emissions from binary RS CVn stars have several components. Of interest are the "core" emissions that come from a small source and, hence, have brightness temperatures greater than 10^{10} K (Lang 1994). These emissions can have high circular polarization, long durations, and restricted bandwidths (Trigilio et al. 1998; Doiron & Mutel 1984; Slee et al. 1984). Models for the core emissions include the electron-cyclotron maser instability. Competing mechanisms include gyrosychrotron emissions.

These long-duration emissions could result from near-continuous electron acceleration or persistent low-amplitude flaring. The complex interaction between the stellar magnetospheres could drive currents that result in nearly persistent particle acceleration. The core emissions have all of the properties of coherent generation by an electron-cyclotron maser. We suggest the shell maser as a possible mechanism for these emissions.

4.4. *Planetary Radiation*

Planetary auroral radiation has been observed from all of the magnetized outer planets (Zarka 1992), which includes Jovian decameteric radiation. Most of the planetary radiation models are derived from the auroral AKR model. These models include acceleration of electrons by a parallel electric field in a dipole magnetic geometry. The application of the shell maser to planetary emissions is particularly compelling in the light of the *FAST* satellite observations.

5. CONCLUSIONS

The electron-cyclotron maser is a well-suited mechanism to explain high brightness temperatures ($>10^{10}$ K), high degrees of circular polarization, and narrow-bandwidth emissions from planetary radiation, solar microwave spikes, and radio bursts from dwarf M flare stars and RS CVn binaries. *FAST* satellite observations have now provided conclusive evidence that the electron-cyclotron maser driven by a shell instability is responsible for the coherent generation of AKR. This finding may necessitate reanalysis of some astrophysical radio sources and allow the electron-cyclotron maser to be applied to radio sources that have not been considered viable in the past; for example, very bright, continuous sources or broadband sources.

To create a shell maser, electrons are accelerated by a near-monoenergetic mechanism. The acceleration energy, (ξ_Φ) is greater than the source temperature ($T_e^{\rm src}$). A magnetic mirror ratio of $R_M > \xi_\Phi / T_e^{\rm src}$ is required so that the electrons adiabatically evolve to higher pitch angles forming a shell. For the instability to occur, the integration surface to determine the imaginary part of the dispersion must form a sphere centered at the origin. The radiation source region must be in a depleted cavity, such that the right cutoff is below ω_{ce} ($\omega_{\rm right} < \omega_{ce}$). The condition for growth is given by $\xi_\Phi / m_e c^2 > 2\gamma^2 \omega_{pe}^2 / \omega_{ce}^2$, where $\omega_{pe} \ll \omega_{ce}$. Simulations and observations do not support the loss cone as the free energy source and demonstrate that the shell maser is a far more powerful radiation source.

Under the shell maser, amplification occurs at frequencies between ω_{ce}/γ and ω_{ce}. The bandwidth of the radiation depends upon the acceleration potential, limited roughly by $(\gamma - 1)/\gamma$. Growth occurs in the X mode with $k_{||} = 0$. The radiation is strongly polarized if it comes from an electron-ion plasma. Amplification occurs in short distances, so source regions can be quite small, resulting in brightness temperatures as high as 10^{20} K. *FAST* satellite observations do not detect generation at higher harmonics in the AKR source region.

The shell instability is not rapidly self-quenching. Amplification can be continuous if the acceleration process is steady. The periods of bursty emissions are determined by the duration of particle acceleration. Because a strong loss cone is not required, the source region is not restricted to a proximity of a stellar or planetary surface. A moderate mirror ratio is required to establish the conditions for amplification. Thus the waves may not experience high harmonic absorption because of lower densities at the shell maser source. *FAST* observations also provide evidence that the radiation is guided within the density cavity and efficiently converted to R-mode emissions. The generation in a density cavity, possibly at higher altitudes, and the conversion to the R mode all conspire to reduce harmonic absorption.

In the AKR source region, particle acceleration is from parallel electric fields. Although one cannot conclude that parallel electric fields uniquely form the shell maser, it is very difficult to envision any other acceleration mechanism that creates the shell distributions and the density-depleted cavities. Thus, one of the most powerful mechanisms of directly amplifying electromagnetic radiation that has been observed in situ is associated with a particular type of charged particle acceleration, parallel electric fields. Parallel electric fields may be more widespread in astrophysical plasmas than currently believed.

The authors wish to thank R. Pottelette, P. Louarn, A. Roux, and G. Dulk for many useful discussions. This work

was funded by NASA under the Fast Auroral Snapshot Mission Operations and Data Analysis at the University of California at Berkeley, the University of California at Los Angeles, and the University of Colorado at Boulder (NAG5-3596).

REFERENCES

Abada-Simon, M., Lecacheux, A., Louarn, P., Dulk, G. A., Belkora, L., Bookbinder, J. A., & Rosolen, C. 1994, A&A, 288, 219
Bahnsen, A. B., Jespersen, M., Ungstrup, E., & Iversen, I. B. 1987, Geophys. Res. Lett., 14, 471
Benz, A. O., Bernold, T. E. X., & Dennis, B. R. 1983, ApJ, 271, 355
Cane, H. V., Stone, R. G., Fainberg, J., Steinberg, J. L., Hoang, S., & Stewart, R. T. 1981, Geophys. Res. Lett., 8, 1285
Carlson, C. W., Pfaff, R. F., & Watzin, J. G. 1998a, Geophys. Res. Lett., 25, 2013
Carlson, C. W., et al. 1998b, Geophys. Res. Lett., 25, 2017
Chiu, Y. T., & Schulz, M. 1978, J. Geophys. Res., 83, 629
Delory, G. T., Ergun, R. E., Carlson, C. W., Muschietti, L., Chaston, C. C., Peria, W., McFadden, J. P., & Strangeway, R. J. 1998, Geophys. Res. Lett., 25, 2069
Doiron, D. J., & Mutel, R. L. 1984, AJ, 89, 430
Ergun, R. E., et al. 1998a, Geophys. Res. Lett., 25, 2061
———. 1998b, Geophys. Res. Lett., 25, 2025
———. 1998c, ApJ, 503, 435
Green, J. L., Gurnett, D. A., & Shawhan, S. D. 1977, J. Geophys. Res., 82, 1825
Gurnett, D. A. 1974, J. Geophys. Res., 79, 4227
Holman, G. D., Eichler, D., & Kundu, M. R. 1980, in IAU Symp. 86, Radio Physics of the Sun, ed. M. Kundu & T. Gergely (Dordrecht: Reidel), 457
Kurth, W. S., Baumback, M. M., & Gurnett, D. A. 1975, J. Geophys. Res., 80, 2764
Lang, K. R. 1994, ApJS, 90, 753
Lang, K. R., Bookbinder, J., Golub, L., & Davis, M. M. 1983, ApJ, 272, L15
Lang, K. R. & Willson, R. F. 1988, ApJ, 326, 300
Lin, R. P., Levedahl, W. K., Lotko, W., Gurnett, D. A., & Scarf, F. L. 1986, ApJ, 308, 954
Louarn, P., Roux, A., de Feraudy, H., Le Queau, D., Andre, M., & Matson, L. 1990, J. Geophys. Res., 95, 5983
McFadden, J. P., et al. 1998, Geophys. Res. Lett., 25, 2021
Melrose, D. B., & Dulk, G. A. 1982, ApJ, 259, 844
Omidi, N., & Gurnett, D. A. 1982, J. Geophys. Res., 88, 2377
Pritchett, P. L. 1984a, Geophys. Res. Lett., 11, 143
———. 1984b, J. Geophys. Res., 89, 8957
Pritchett, P. L., & Strangeway, R. J. 1985, J. Geophys. Res., 90, 9650
Pritchett, P. L., Strangeway, R. J., Carlson, C. W., Ergun, R. E., McFadden, J. P., & Delory, G. T. 1999, J. Geophys. Res., 104, 10317
Robinson, P. A. 1989, ApJ, 341, L99
Roux, A., Hilgers, A., de Feraudy, H., Le Queau, D., Louarn, P., & Perraut, S. 1993, J. Geophys. Res., 98, 11657
Slee, O. B., Haynes, R. F., & Wright, A. E. 1984, MNRAS, 208, 865
Stepanov, A. V., Fuerst, E., Krueger, A., Hildebrandt, J., Barwig, H., & Schmitt, J. 1995, A&A, 299, 739
Strangeway, R. J., et al. 1998, Geophys. Res. Lett., 25, 2065
Trigilio, C., Leto, P., & Umana, G. 1998, A&A, 330, 1060
Tsui, K. H. 1996, Sol. Phys., 168, 171
White, S. M., Melrose, D. B., & Dulk, G. A. 1983, Proc. Astron. Soc. Australia, 5(2), 188
Willes, A. J., & Robinson, P. A. 1996, ApJ, 467, 465
Willson, R. F. 1985, Sol. Phys., 96, 199
Winglee, R. M., & Dulk, G. A. 1986, ApJ, 310, 432
Winglee, R. W., & Pritchett, P. L. 1986, J. Geophys. Res., 91, 13531
Wu, C. S., & Lee, L. C. 1979, ApJ, 230, 621
Zarka, P. 1992, Adv. Space Res., 12 (8), 99